LETTER

doi:10.1038/nature15747

The first stars formed soon after the plasma to gas transition at 0.3 Myr, not 200 Myr. CHG

Extremely metal-poor stars from the cosmic dawn in the bulge of the Milky Way

See journalofcosmology.com Vol 25 etc.

L. M. Howes[1], A. R. Casey[2], M. Asplund[1], S. C. Keller[1], D. Yong[1], D. M. Nataf[1], R. Poleski[3,4], K. Lind[5], C. Kobayashi[1,6], C. I. Owen[1], M. Ness[7], M. S. Bessell[1], G. S. Da Costa[1], B. P. Schmidt[1], P. Tisserand[1,8], A. Udalski[3], M. K. Szymański[3], I. Soszyński[3], G. Pietrzyński[3,9], K. Ulaczyk[3,10], Ł. Wyrzykowski[3], P. Pietrukowicz[3], J. Skowron[3], S. Kozłowski[3] & P. Mróz[3]

Failure to predict star formation is one of many failures of LCDMHC cosmology vs. HGD.

The first stars are predicted to have formed within 200 million years after the Big Bang[1], initiating the cosmic dawn. A true first star has not yet been discovered, although stars[2–4] with tiny amounts of elements heavier than helium ('metals') have been found in the outer regions ('halo') of the Milky Way. The first stars and their immediate successors should, however, preferentially be found today in the central regions ('bulges') of galaxies, because they formed in the largest over-densities that grew gravitationally with time[5,6]. The Milky Way bulge underwent a rapid chemical enrichment during the first 1–2 billion years[7], leading to a dearth of early, metal-poor stars[8,9]. Here we report observations of extremely metal-poor stars in the Milky Way bulge, including one star with an iron abundance about 10,000 times lower than the solar value without noticeable carbon enhancement. We confirm that most of the metal-poor bulge stars are on tight orbits around the Galactic Centre, rather than being halo stars passing through the bulge, as expected for stars formed at redshifts greater than 15. Their chemical compositions are in general similar to typical halo stars of the same metallicity although intriguing differences exist, including lower abundances of carbon.

Stars with a low content of heavy elements have distinct spectral flux distributions, which are reflected in their colours. Using the photometric filter system on the SkyMapper telescope operated by the Australian National University, it is possible to identify metal-poor candidate stars[10] in the Galactic halo[4] and bulge[9]. We have observed ~14,000 bulge stars preselected from SkyMapper photometry using the AAOmega spectrograph on the Anglo-Australian Telescope (AAT), which enables the acquisition of 400 simultaneous stellar spectra over a 2-degree field of view. More than 500 stars with an iron abundance less than 1/100th of the solar value have been identified, making our survey the first to successfully target metal-poor stars in the Milky Way bulge. Twenty-three of these stars, targeted as the most metal-poor ones on the basis of the intermediate resolution spectra (Extended Data Table 1), were observed in June 2014 with the MIKE high-resolution spectrograph on the 6.5-m Magellan Clay telescope[11] to enable a comprehensive determination of their chemical compositions (Fig. 1).

The stars' effective temperatures were derived through fitting the observed hydrogen lines with theoretical spectra, while neutral and ionized iron lines provided measurements of the surface gravities and metallicities in the framework of 1D stellar atmosphere models[12] and non-equilibrium spectral line formation[13] (Extended Data Table 2). All 23 stars were found to have [Fe/H] ≤ -2.3, including nine stars with [Fe/H] < -3 (here $[A/B] = \log_{10}(N_A/N_B)_* - \log_{10}(N_A/N_B)_\odot$, where N_A/N_B refers to the number ratio of atoms of elements A and B in the star ($*$ subscript) and the Sun ($\odot$ subscript)). The most metal-poor star, SMSS J181609.62−333218.7, has [Fe/H] $= -3.94 \pm 0.16$. The abundances of an additional 22 elements were determined spectroscopically, including the α-elements Mg, Si, Ca, and Ti, and the neutron-capture elements Y, Zr, and Ba (Extended Data Tab

The bulge density decreases with time due to the expansion of the universe.

To cor… of the stars have been determined. Using the spectroscopic temperatures and surface gravities, and an assumed mass of $0.8M_\odot$, distances were inferred, which in nearly all cases are consistent with them being located within the bulge (Fig. 2). We have measured velocities for ten of ou… whic… tion… rema… kinematic information are too uncertain to constrain the orbits sufficiently. Seven out of the ten stars with accurate kinematics are shown to have tightly bound orbits, placing them in the inner regions of the Milky Way (Fig. 2). In particular, using a cut-off radius of 3.43 kpc as the radius of the bulge component[15], the most metal-poor star SMSS J181609.62−333218.7 has an orbit entirely contained within the bulge. Only two out of the ten stars are on much larger orbits, being merely halo stars currently passing through the bulge region. Extending these numbers to the whole sample, we can expect ~14 of the 23 bulge stars analysed here to have orbits fully within the central regions of the Milky Way; with the imminent arrival of kinematic data from the Gaia satellite, accurate orbits for all of the bulge stars will be able to be determined.

Interesting observations that confirm hydro-gravitational-dynamics HGD cosmology vs. LCDMHC (failed) cosmology.

The very first stars are predicted to have brought about the cosmic dawn by forming in the centres of the largest dark matter mini-haloes, which subsequently accreted material to become the inner regions of the largest galaxies[16]. The typical redshift of formation for stars in the … $z \approx 5$ for halo stars. Of … % are expected to have … h accurate orbit infor… $< -8 \times 10^{-4}$ km^2 s^{-2}, which is consistent with a formation redshift of $z > 15$ (ref. 5). Low binding energies imply that the stars have been in the Galactic potential well for some time and it is very unlikely they have been accreted from a recent dwarf spheroidal merger. Their low metallicities, orbits and binding energies make these stars prime candidates for being direct descendants of the very first stars, probing a cosmic epoch otherwise completely inaccessible currently. Direct age determinations of these ancient and extremely metal-poor bulge stars from comparison with stellar evolutionary tracks or radioactive U or Th dating are currently not possible, but asteroseismic ages could possibly be inferred with the extended Kepler mission or future satellites.

There is no cold dark matter so it cannot clump, and there are no minihalos.

[1]Research School of Astronomy and Astrophysics, Australian National University, Australian Capital Territory 2601, Australia. [2]Institute of Astronomy, University of Cambridge, Madingley Road, Cambridge CB3 0HA, UK. [3]Warsaw University Observatory, Aleje Ujazdowskie 4, 00-478 Warszawa, Poland. [4]Department of Astronomy, Ohio State University, 140 West 18th Avenue, Columbus, Ohio 43210, USA. [5]Department of Physics and Astronomy, Division of Astronomy and Space Physics, Uppsala University, Box 516, SE-751 20 Uppsala, Sweden. [6]School of Physics, Astronomy and Mathematics, Centre for Astrophysics Research, University of Hertfordshire, College Lane, Hatfield AL10 9AB, UK. [7]Max-Planck-Institut für Astronomie, Königstuhl 17, D-69117 Heidelberg, Germany. [8]Sorbonne Universités, UPMC Université Paris 6 et CNRS, UMR 7095, Institut d'Astrophysique de Paris, 98 bis Boulevard Arago, 75014 Paris, France. [9]Universidad de Concepción, Departamento de Astronomia, Casilla 160-C, Concepción, Chile. [10]Department of Physics, University of Warwick, Gibbet Hill Road, Coventry CV4 7AL, UK.

Journal of Cosmology (2015), Vol. 25, No. 32, pp 13613-13625.

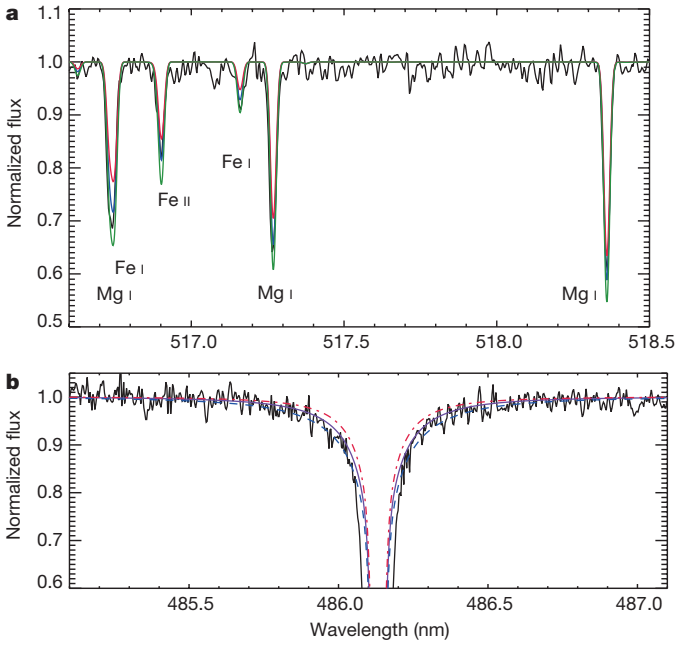

Figure 1 | Extracts of the spectrum of the lowest-metallicity star in our sample. a, A section of the spectrum of SMSS J181609.62−333218.7 (black line), the most metal-poor bulge star known. In blue is the predicted spectrum with the inferred stellar parameters (effective temperature $T_{\rm eff}=4{,}809$ K, $\log(g)=1.93$ (here surface gravity g is in cgs units), [Fe/H] = −3.94, [Mg/Fe] = 0.20), and the red and green lines show spectra with all abundances scaled to ± 0.15 dex, respectively. All three predicted spectra were created using the 1D local thermodynamic equilibrium (LTE) spectrum synthesis programme, MOOG[26]. **b**, The Hβ line of the same star, compared to three synthetic spectral line profiles[27] computed with $T_{\rm eff}=4{,}640$ K (red, dash-dot), 4,800 K (purple, continuous), and 4,960 K (blue, dashed).

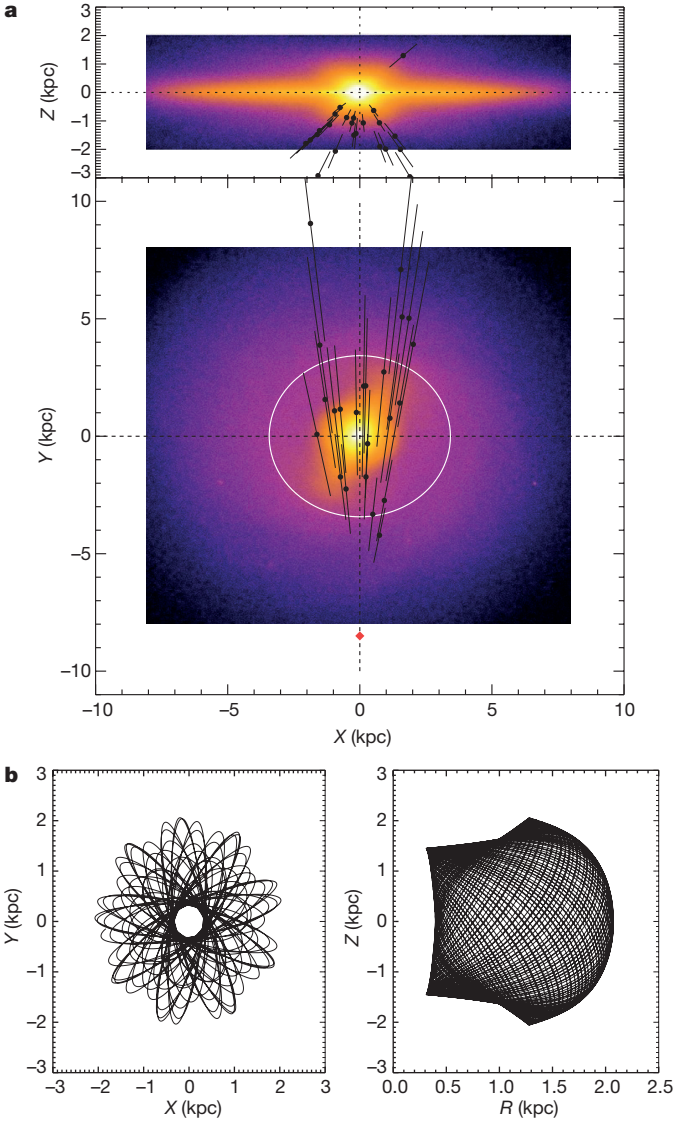

Figure 2 | The Galactic positions and orbits of the 23 stars observed at high resolution. a, Surface density map of a model of the Galactic bulge projected onto the X–Z (top) and X–Y (bottom) planes[28], where X, Y, and Z are Cartesian coordinates with the origin at the Galactic Centre and Z perpendicular to the plane of the Galaxy. Plotted over this (filled black circles) are the 23 stars of this study, with distance uncertainties shown as error bars, and a circle of radius 3.43 kpc (white: the cut-off radius of the inner bulge determined from 2MASS data[15]). The position of the Sun is shown with a red diamond, at 8.5 kpc from the Galactic Centre. **b**, Projections of the orbit of the lowest metallicity star, SMSS J181609.62−333218.7, both in the (R, Z) plane (right), where R is the radial direction, and in the plane of the orbit itself (left).

Given their extremely low metallicities and large formation redshifts, these stars are likely to have formed from gas polluted by ejecta from a single or at most a few supernovae of the first stellar generation. A chemical composition analysis has been carried out to search for tell-tale nucleosynthetic signatures and possible differences from halo stars at the same metallicities. For most elements, the chemical compositions of the 23 bulge stars are consistent with typical halo stars, suggesting enrichment by similar supernovae in spite of the distinct environments and formation redshifts. Subtle differences do exist however, most notably in terms of the carbon abundances. None of the 23 stars have the large observed carbon enhancements that occur frequently in halo stars. Applying evolutionary corrections to the surface carbon abundance to counter the mixing that occurs with material processed by H-burning through CNO-cycling at late stages of the stellar lifetime[17], still only one of the stars would have had a natal [C/Fe] > 1. In the halo, the percentage of stars that are carbon-enhanced increases dramatically at lower metallicities—from 27% of stars with [Fe/H] < −2 up to 69% with [Fe/H] < −4 (ref. 17). From the literature data on halo stars with similar iron abundances to our stars[17], the probability of selecting at most one carbon-enhanced star out of 23 halo stars is only 0.2%. Carbon-enhanced stars come in two varieties: those with and those without large excesses of neutron-capture elements. The former are most likely to have been formed by mass-transfer from a binary companion that underwent the asymptotic giant branch phase. Those carbon-enhanced stars with neutron-capture excesses occur most frequently at metallicities of [Fe/H] > −3, whereas those without do not appear to have binary companions, and are more common at the very lowest metallicities. As none of our bulge stars are classified as having large abundances of neutron capture elements, the likelihood of finding one such carbon-enhanced star out of 23 is 7% if the frequency is the same for the bulge as for the halo. A lower frequency of carbon-enhanced stars in the bulge relative to the halo is contrary to theoretical predictions; the expected dependence of the initial mass function on the cosmic microwave background[18] would result in a greater number of carbon-enhanced stars near the centre of the Galaxy.

The most metal-poor bulge star, SMSS J181609.62−333218.7, is at least an order of magnitude more iron-deficient than previously found low-metallicity bulge stars[9,19]. We have not been able to detect C in its spectrum, instead finding only an upper limit to its C abundance (Extended Data Fig. 1). This makes the upper limit on its total metallicity [Z/H] ≈ −3.8 (total mass fraction of $Z \approx 2.1 \times 10^{-6}$), where Z represents the sum of all metals, placing it amongst the four most metal-poor stars known, along with the halo star SDSS J102915+172927 (ref. 3). The low C measured in both these stars fall below the predicted

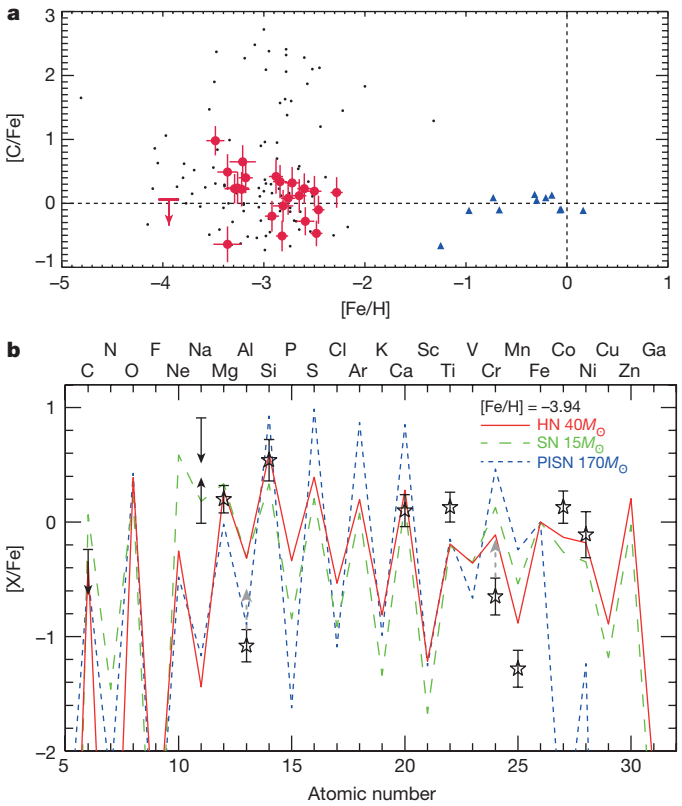

Figure 3 | Chemical abundances of the 23 stars observed at high resolution. a, The abundance ratio of carbon versus iron ([C/Fe]), with respect to metallicity ([Fe/H]) measured in the observed stars (filled red circles, red arrow for an upper limit). The dotted lines represent the solar abundances. Also shown for comparison are literature metal-poor halo giants (small black dots[24]) and more metal-rich bulge stars (filled blue triangles[29]). **b**, The chemical abundance pattern of SMSS J181609.62−333218.7, for elements X, where X is displayed at the top of the figure. Each determined abundance is shown as an open black star. These abundances are compared to three synthetic supernovae yields: a pair-instability supernova of 170$M_\odot$ (PISN; blue, short dash[22]), a core-collapse supernova of 15$M_\odot$ (SN: green, long dash[21]), and a hypernova of 40$M_\odot$ (HN; red, solid[21]). Dashed grey arrows represent expected non-LTE corrections; solid arrows represent measurements where only an upper or lower limit was possible. The error bars in **a** and **b** are estimates of the uncertainties in our measurements, calculated as described in Methods.

metallicity limit for formation of low-mass stars due to metal line cooling[20].

We have compared the detailed chemical abundance pattern of SMSS J181609.62−333218.7 to primordial supernovae yields[21,22] (Fig. 3). In particular, the low Mg and Ca abundance, but higher Si abundance, and the absence of a pronounced odd–even abundance pattern rule out the possibility of enrichment by a pair-instability supernova resulting from a primordial star of (140–250)$M_\odot$. Low abundances of Cr and Mn and of α-elements, combined with the higher abundance of Co, indicate that the polluting supernova was most likely to have been a primordial hypernova—an extremely energetic kind of supernova releasing ten times the kinetic energy of regular core-collapse supernovae, possibly due to the forming black hole having larger angular momentum[23]. Good agreement is found for a 40$M_\odot$ hypernova; a more stringent Zn limit would further constrain the mass range. Unusual abundance ratios have been found in small numbers of stars in the halo—4% of halo stars with low carbon abundances have chemical peculiarities in at least two elements[24]—but none so far appear to have been polluted by a 40$M_\odot$ hypernova. A low [α/Fe] ratio (0.14 dex; here α indicates α-elements) at such low [Fe/H] is consistent with an inhomogeneous enrichment from such supernovae[25], while stars with higher [α/Fe] formed from more well-mixed gas due to a longer time delay in forming the second generation of stars.

Online Content Methods, along with any additional Extended Data display items and Source Data, are available in the online version of the paper; references unique to these sections appear only in the online paper.

Received 1 May; accepted 24 August 2015.
Published online 11 November 2015.

1. Bromm, V., Yoshida, N., Hernquist, L. & McKee, C. F. The formation of the first stars and galaxies. *Nature* **459,** 49–54 (2009).
2. Christlieb, N. *et al.* A stellar relic from the early Milky Way. *Nature* **419,** 904–906 (2002).
3. Caffau, E. *et al.* An extremely primitive star in the Galactic halo. *Nature* **477,** 67–69 (2011).
4. Keller, S. C. *et al.* A single low-energy iron-poor supernova as the source of metals in the star SMSS J031300.36–670839.3. *Nature* **506,** 463–466 (2014).
5. Tumlinson, J. Chemical evolution in hierarchical models of cosmic structure. II. The formation of the Milky Way stellar halo and the distribution of the oldest stars. *Astrophys. J.* **708,** 1398–1418 (2010).
6. Salvadori, S., Ferrara, A., Schneider, R., Scannapieco, E. & Kawata, D. Mining the Galactic halo for very metal-poor stars. *Mon. Not. R. Astron. Soc.* **401,** L5–L9 (2010).
7. Feltzing, S. & Gilmore, G. Age and metallicity gradients in the Galactic bulge. *Astrophys. Space Sci.* **265,** 337–340 (1999).
8. García Pérez, A. E. *et al.* Very metal-poor stars in the outer Galactic bulge found by the APOGEE survey. *Astrophys. J.* **767,** L9 (2013).
9. Howes, L. M. *et al.* The Gaia-ESO survey: the most metal-poor stars in the Galactic bulge. *Mon. Not. R. Astron. Soc.* **445,** 4241–4246 (2014).
10. Keller, S. C. *et al.* The SkyMapper Telescope and the Southern Sky Survey. *Publ. Astron. Soc. Aust.* **24,** 1–12 (2007).
11. Bernstein, R., Shectman, S. A., Gunnels, S. M., Mochnacki, S. & Athey, A. E. MIKE: a double echelle spectrograph for the Magellan Telescopes at Las Campanas Observatory. *Proc. SPIE* **4841,** 1694–1704 (2003).
12. Gustafsson, B. *et al.* A grid of MARCS model atmospheres for late-type stars. *Astron. Astrophys.* **486,** 951–970 (2008).
13. Lind, K., Bergemann, M. & Asplund, M. Non-LTE line formation of Fe in late-type stars — II. 1D spectroscopic stellar parameters. *Mon. Not. R. Astron. Soc.* **427,** 50–60 (2012).
14. Udalski, A., Szymański, M. K. & Szymański, G. OGLE-IV: fourth phase of the Optical Gravitational Lensing Experiment. *Acta Astron.* **65,** 1–38 (2015).
15. Robin, A. C., Marshall, D. J., Schultheis, M. & Reylé, C. Stellar populations in the Milky Way bulge region: towards solving the Galactic bulge and bar shapes using 2MASS data. *Astron. Astrophys.* **538,** A106–A120 (2012).
16. Greif, T. H. *et al.* Formation and evolution of primordial protostellar systems. *Mon. Not. R. Astron. Soc.* **424,** 399–415 (2012).
17. Placco, V. M., Frebel, A., Beers, T. C. & Stancliffe, R. J. Carbon-enhanced metal-poor star frequencies in the Galaxy: corrections for the effect of evolutionary status on carbon abundances. *Astrophys. J.* **797,** 21 (2014).
18. Tumlinson, J. Carbon-enhanced metal-poor stars, the cosmic microwave background, and the stellar initial mass function in the early universe. *Astrophys. J.* **664,** L63–L66 (2007).
19. Schlaufman, K. C. & Casey, A. R. The best and brightest metal-poor stars. *Astrophys. J.* **797,** 13 (2014).
20. Frebel, A., Johnson, J. L. & Bromm, V. Probing the formation of the first low-mass stars with stellar archaeology. *Mon. Not. R. Astron. Soc.* **380,** L40–L44 (2007).
21. Kobayashi, C., Ishigaki, M. N., Tominaga, N. & Nomoto, K. The origin of low [α/Fe] ratios in extremely metal-poor stars. *Astrophys. J.* **785,** L5 (2014).
22. Umeda, H. & Nomoto, K. Nucleosynthesis of zinc and iron peak elements in population III type II supernovae: comparison with abundances of very metal poor halo stars. *Astrophys. J.* **565,** 385–404 (2002).
23. Nomoto, K. *et al.* Nucleosynthesis in black-hole-forming supernovae and extremely metal-poor stars. *Prog. Theor. Phys.* **151** (Suppl.), 44–53 (2003).
24. Yong, D. *et al.* The most metal-poor stars. II. Chemical abundances of 190 metal-poor stars including 10 new stars with [Fe/H] ≤ –3.5. *Astrophys. J.* **762,** 26–63 (2013).
25. Karlsson, T., Bromm, V. & Bland-Hawthorn, J. Pregalactic metal enrichment: the chemical signatures of the first stars. *Rev. Mod. Phys.* **85,** 809–848 (2013).
26. Sneden, C., Bean, J., Ivans, I., Lucatello, S. & Sobeck, J. MOOG: LTE line analysis and spectrum synthesis. *Astrophysics Source Code Library* http://adsabs.harvard.edu/abs/2012ascl.soft02009S (2012)
27. Barklem, P. S., Piskunov, N. & O'Mara, B. J. Self-broadening in Balmer line wing formation in stellar atmospheres. *Astron. Astrophys.* **363,** 1091–1105 (2000).
28. Ness, M. *et al.* Young stars in an old bulge: a natural outcome of internal evolution in the Milky Way. *Astrophys. J.* **787,** L19 (2014).
29. Ryde, N. *et al.* Chemical abundances of 11 bulge stars from high-resolution, near-IR spectra. *Astron. Astrophys.* **509,** A20–A35 (2010).

Acknowledgements This paper includes data gathered with the 6.5-m Magellan Telescopes located at Las Campanas Observatory, Chile. Australian access to the Magellan Telescopes was supported through the Collaborative Research Infrastructure Strategy of the Australian Federal Government. L.M.H. and M.A.

were supported by the Australian Research Council (FL110100012). A.R.C. acknowledges support from the European Union FP7 programme through ERC grant number 320360. Research on metal-poor stars with SkyMapper is supported through Australian Research Council Discovery Projects grants DP120101237 and DP150103294 (principal investigator G.S.D.C.). The OGLE project received funding from the NSC, Poland (MAESTRO grant 2014/14/A/ST9/00121 to A.U.).

Author Contributions The project was initiated and led by M.A. The photometric target selection was made by L.M.H., C.I.O. and D.M.N. using data from the SkyMapper telescope developed by B.P.S., S.C.K., G.S.D.C., M.S.B. and P.T. The low-resolution spectra were obtained by L.M.H and C.I.O. The data were reduced and analysed by L.M.H. using software developed by A.R.C. Target selection for the high-resolution observations was done by L.M.H., M.A. and A.R.C. with the observations carried out by L.M.H. and D.Y.; the reduction and subsequent chemical analysis was completed by L.M.H. K.L. performed the non-LTE spectral line formation calculations, C.K. interpreted the observed chemical abundances in terms of supernova yields, and M.N. provided comparison bulge data. R.P., A.U., M.K.S, I.S., G.P., K.U., Ł.W., P.P., J.S., S.K. and P.M. obtained the OGLE observations, A.U. and M.K.S. constructed the reference images, and R.P. measured the proper motions. The manuscript was written by M.A., L.M.H. and A.R.C. with all authors contributing comments.

Author Information Reprints and permissions information is available at www.nature.com/reprints. The authors declare no competing financial interests. Readers are welcome to comment on the online version of the paper. Correspondence and requests for materials should be addressed to L.M.H. (louise.howes@anu.edu.au).

It is quite impossible to sensibly discuss the cosmic dawn starting with the nonsense cosmology LCDMHC that ignores fluid mechanics by assuming all processes of the universe are collisionless. Stars are formed as soon as the plasma turns to gas at 10^13 seconds after the big bang. The plasma fragments to form protogalaxies at the Kolmogorov-Nomura scale of 10^20 meters at 10^12 seconds and the nonbaryonic dark matter begins to diffuse away because it is so weakly collisional. The missing mass of galaxies was discovered by Schild (1996) by microlensing of a quasar by a galaxy. The dark matter objects weighed ~ 10^24 kg, and formed in Jeans mass clumps of a trillion from fluid mechanical arguments of Gibson (1996). All stars are formed by binary accretion of these planets within the clumps. The clumps are called protoglobularstarclusters because when all the planets merge they are observed as globular star clusters. Infrared telescopes such as Planck and Herschel have detailed the formation of stars within PGCs. HGD cosmology is an observational fact. LCDMHC cosmology has been repeatedly falsified and belongs with speculations that the Earth is flat and that it is not necessary for doctors to wash their hands between operations.

METHODS

Observations. Photometry of the Milky Way bulge was acquired for the EMBLA survey[9] during the commissioning period of the SkyMapper telescope in 2012 and 2013. Stars were selected from the photometry using a combination of the *g*, *i*, and *v* bandpasses, designed to give a reliable metallicity indicator[10].

Spectroscopic follow-up observations took place during 2012–14, making use of the AAOmega+2dF multi-object spectrograph[30] on the Anglo-Australian Telescope. With between 350 and 400 stars observed in each field, spectra of more than 14,000 bulge stars have been obtained. The gratings used have a spectral resolving power of 1,300 in the blue (370–580 nm) and 10,000 in the red (840–885 nm). The data were reduced using the standard 2dfdr pipeline. Stellar spectra were fitted using a generative model that simultaneously accounts for stellar parameters (by interpolating from the AMBRE grid[31]), continuum, spectral resolution and radial velocity.

From the first two years of spectroscopic data, more than 50 stars were identified as having [Fe/H] < -2.5. The high-resolution spectroscopic data of 23 stars presented in this Letter are the result of observations using the MIKE spectrograph at the Magellan Clay telescope[11] on 15–17 June 2014. All observations were taken using a slit width of 0.7″, resulting in a resolving power of 35,000 in the blue and 31,000 in the red. The data were reduced using the CarPy data reduction pipeline[32], before they were normalized and summed together using the SMH software[33]. The final spectra cover 330–890 nm.

Parameter and abundance determination. The stellar parameters (Extended Data Table 2) were calculated iteratively, using the original parameters from the low-resolution spectra as initial guesses. First, effective temperatures were derived by fitting the wings of the Balmer Hα and Hβ lines with a synthetic profile (Fig. 1). These profiles were created by linearly interpolating between a grid of synthetic spectra[27]. The best lines were fitted by a χ^2 minimization, using a weighted average of the two lines—weighting was double on the Hβ line, due to predicted LTE effects being larger for Hα (ref. 34). The difference between the temperatures calculated for each line was on average only 26 K. The log(*g*), microturbulence ξ_t, and [Fe/H] were then derived for that temperature, by forcing the Fe I abundance to remain constant with respect to reduced equivalent width, and equilibrium between the Fe I and Fe II abundances. Fe I and Fe II abundances were measured from the equivalent widths of a maximum of 66 Fe I lines and 24 Fe II lines (in the case of the most metal-poor star, SMSS J181609.62−333218.7, these numbers are reduced to 10 Fe I lines and 4 Fe II lines). Finally a non-LTE correction is applied to the Fe I abundance, calculated by taking the average of the line-by-line corrections[12]. This correction forces an offset between the Fe I and Fe II abundances, thus replacing the initial equilibrium. This process is repeated until the parameters converge on a solution. Throughout we use the 1D MARCS model atmospheres[13], and a shortened version of the Gaia-ESO line list, with extra lines supplemented from ref. 35 due to our wider wavelength coverage. The stellar abundances are referenced to the solar abundances of ref. 36. This analysis method was tested on seven halo stars from the literature[25], and the offsets found were $T_{\rm eff} = +28$ K, log(*g*) $= -0.2$, and [Fe/H] $= -0.08$ (literature values minus our values).

The abundances were measured using the equivalent widths of atomic lines (that were all on the linear part of the curve-of-growth), except in the case of C (measured from the C–H molecular bands at 431.3 nm and 432.3 nm) and Ba (synthesized in order to account for hyperfine splitting). Non-LTE corrections were calculated for Li (ref. 37), Na (ref. 38), Mg, and Ca, and applied to the individual line abundances. The literature halo abundances of Mg and Ca (ref. 25) shown in Fig. 3 have also had a NLTE correction applied, in order to ensure a fair comparison. 3σ upper limits were derived for some elements in those stars where the lines were too weak to be detected (Extended Data Table 3). The abundance offsets compared to the literature values averaged 0.10 ± 0.19 across those elements measured in common. Owing to wavelengths covered in the SkyMapper metallicity filter, it is possible that stars with extremely high C abundance appeared to be more metal-rich, and so were not selected. However, a similar study of metal-poor stars discovered in the halo with SkyMapper[39] found the fraction of C-enhanced stars was identical to that reported in previous surveys[40]. Furthermore, we followed up 14,000 stars with intermediate resolution spectra, and determined metallicities using those spectra. The majority of the stars observed had [Fe/H] ≈ -1.0 and included some that had solar metallicities, so it is highly unlikely that we missed any C-enhanced extremely metal-poor stars in our selection.

The systematic uncertainties in the temperature determinations were estimated to be ± 100 K, and the statistical uncertainties averaged ± 125 K, so when these are combined in quadrature we conclude the total uncertainty to be ± 160 K. The ξ_t uncertainties are estimated to be ± 0.2, mostly due to systematics.

The standard errors of the individual line abundances of Fe I and Fe II were combined in quadrature to evaluate the log(*g*) uncertainties. The differences between the [Fe/H] values when varying the temperature, surface gravity, and microturbulence by their respective errors were combined in quadrature with the standard error of the Fe II lines to produce the [Fe/H] uncertainties. The individual abundance errors were also calculated using this method, using the standard error of the individual abundances for the lines of that particular element.

For SMSS J181609.62−333218.7, which has [Fe/H] $= -3.94$, a measurement of Na was not possible, owing to the 818.3 nm and 819.4 nm lines being too weak, and the Na D lines (588.9 nm and 589.5 nm) being partly blended with interstellar Na lines. We have derived a range of possible values for this star, taking the upper limit from the non-detection at 819.4 nm, and the lower limit from fitting a Gaussian to the Na D lines, taking into account the interstellar Na.

Distances and orbital parameters. Distances to the stars were calculated by comparing the absolute and apparent bolometric magnitudes. The absolute magnitudes were recovered from the relation $M_* = M_\odot - 2.5\log(L_*/L_\odot)$, where the luminosities are calculated using $L_*/L_\odot = 4\pi\sigma T^4 M_* G / 10^{\log(g_*)}$, taking $M_* = (0.8 \pm 0.2) M_\odot$ for all stars. The apparent bolometric magnitudes are reconstructed from the 2MASS JHK_s magnitudes (Extended Data Table 1), assuming reddening[41] (as no more-recent reddening catalogue covers all 23 stars), via the methodology of ref. 42. The proper motions are based on I band images taken during the OGLE-IV[14] observations of the Galactic bulge. Relative proper motions were derived from multiple epochs of data for each field[43], and the uncertainties are a combination of statistical and systematic (for each star, the systematic uncertainty is estimated to be ~0.4 mas yr^{-1}). These were converted into absolute proper motions by adding the predicted average bulge motion for each field, calculated using the Besancon Galaxy model[44]. The orbits were calculated using the python package galpy[45] and the galactic potential assumed in these calculations was a three-component Milky Way-like potential[46]. To model the uncertainty distributions, we sampled 1,000 orbits using a Monte Carlo simulation, assuming a normal distribution for the uncertainties of the input parameters. The results of this are included in Extended Data Table 6. One star, SMSS J175455.52 – 380339.3, has an unbound $E_{\rm tot}$ and impractically large orbital parameters, suggesting that one or more of our input parameters need to be changed.

Code availability. All codes used to analyse the data presented are publicly available. In particular, the 1D LTE analysis used was made possible with the line analysis and spectrum synthesis code MOOG[26].

30. Sharp, R. *et al.* Performance of AAOmega: the AAT multi-purpose fiberfed spectrograph. *Proc. SPIE* **6269,** 1–13 (2006).
31. de Laverny, P., Recio-Blanco, A., Worley, C. C. & Plez, B. The AMBRE project: a new synthetic grid of high-resolution FGKM stellar spectra. *Astron. Astrophys.* **544,** A126–A137 (2012).
32. Kelson, D. MIKE pipeline http://code.obs.carnegiescience.edu/mike (2014).
33. Casey, A. R. A tale of tidal tails in the Milky Way. Preprint at http://arXiv.org/abs/1405.5968 (2014).
34. Barklem, P. S. Non-LTE Balmer line formation in late-type spectra: effects of atomic processes involving hydrogen atoms. *Astron. Astrophys.* **466,** 327–337 (2007).
35. Norris, J. E. *et al.* The most metal-poor stars. I. Discovery, data, and atmospheric parameters. *Astrophys. J.* **762,** 25 (2013).
36. Asplund, M., Grevesse, N., Sauval, A. J. & Scott, P. The chemical composition of the Sun. *Annu. Rev. Astron. Astrophys.* **47,** 481–522 (2009).
37. Lind, K., Asplund, M. & Barklem, P. S. Departures from LTE for neutral Li in late-type stars. *Astron. Astrophys.* **503,** 541–544 (2009).
38. Lind, K., Asplund, M., Barklem, P. S. & Belyaev, A. K. Non-LTE calculations for neutral Na in late-type stars using improved atomic data. *Astron. Astrophys.* **528,** A103–A112 (2011).
39. Jacobson, H. R. *et al.* High-resolution spectroscopic study of extremely metal-poor star candidates from the SkyMapper survey. *Astrophys. J.* **807,** 171 (2015).
40. Lucatello, S. *et al.* The frequency of carbon-enhanced metal-poor stars in the Galaxy from the HERES sample. *Astrophys. J.* **652,** L37–L40 (2006).
41. Schlegel, D. J., Finkbeiner, D. P. & Davis, M. Maps of dust infrared emission for use in estimation of reddening and cosmic microwave background radiation foregrounds. *Astrophys. J.* **500,** 525–553 (1998).
42. Casagrande, L., Portinari, L. & Flynn, C. Accurate fundamental parameters for lower main-sequence stars. *Mon. Not. R. Astron. Soc.* **373,** 13–44 (2006).
43. Poleski, R. *et al.* An asymmetric streaming motion in the Galactic bulge X-shaped structure revealed by OGLE-III proper motions. *Astrophys. J.* **776,** 76 (2013).
44. Robin, A. C., Reylé, C., Derrière, S. & Picaud, S. A synthetic view on structure and evolution of the Milky Way. *Astron. Astrophys.* **409,** 523–540 (2003).
45. Bovey, J. *galpy* http://github.com/jobovy/galpy (2015).
46. Bovy, J. galpy: A python library for galactic dynamics. *Astrophys. J.* **216,** 29 (2015).

Journal of Cosmology (2015), Vol. 25, No. 32, pp 13613-13625.

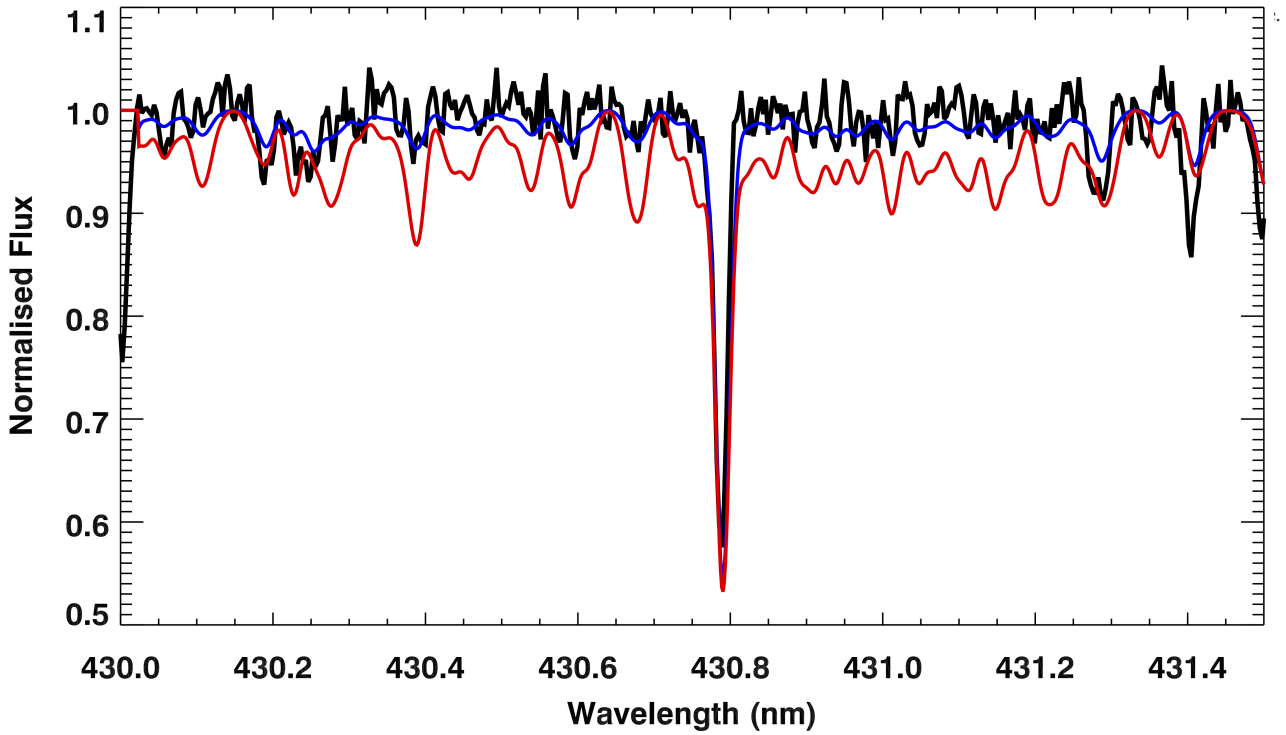

Extended Data Figure 1 | The C–H band of SMSS J181609.62 – 333218.7. The C–H band is used to derive an upper limit for C in our most metal-poor star, SMSS J181609.62 – 333218.7. Synthetic spectra with abundances of [C/Fe] = 0.06 (blue) and [C/Fe] = 0.56 (red) are shown for comparison.

Extended Data Table 1 | Coordinates and 2MASS photometry of the 23 stars observed

Name (SMSS)	RA (°)	Dec (°)	l (°)	b (°)	J (mag)	H (mag)	K_S (mag)
J173823.38-145701.1	264.597	-14.950	11.1	8.7	10.85	10.22	10.03
J182048.26-273329.2	275.201	-27.558	5.0	-6.1	12.94	12.42	12.25
J183744.90-280831.1	279.437	-28.142	6.2	-9.7	12.29	11.69	11.53
J183647.89-274333.1	279.200	-27.726	6.5	-9.3	10.68	10.03	9.77
J183812.72-270746.3	279.553	-27.130	7.1	-9.3	13.38	12.79	12.61
J183719.09-262725.0	279.330	-26.457	7.7	-8.9	12.79	12.19	12.03
J184201.19-302159.6	280.505	-30.367	4.5	-11.5	14.52	14.08	14.00
J184656.07-292351.5	281.734	-29.398	5.9	-12.0	13.12	12.61	12.51
J181406.68-313106.1	273.528	-31.518	0.8	-6.6	12.12	11.56	11.35
J181317.69-343801.9	273.324	-34.634	357.9	-7.9	13.09	12.55	12.50
J181219.68-343726.4	273.082	-34.624	357.9	-7.7	12.80	12.28	12.15
J181609.62-333218.7	274.040	-33.539	359.2	-7.9	13.39	12.84	12.71
J181634.60-340342.5	274.144	-34.062	358.8	-8.3	12.56	11.99	11.90
J175544.54-392700.9	268.936	-39.450	352.0	-7.1	13.71	13.19	13.09
J175455.52-380339.3	268.731	-38.061	353.1	-6.3	11.98	11.39	11.26
J175746.58-384750.0	269.444	-38.797	352.8	-7.2	13.09	12.60	12.51
J181736.59-391303.3	274.402	-39.218	354.2	-10.8	12.06	11.54	11.37
J181505.16-385514.9	273.772	-38.921	354.2	-10.2	13.63	13.15	13.09
J181921.64-381429.0	274.840	-38.241	355.2	-10.6	13.64	13.13	13.03
J175722.68-411731.8	269.345	-41.292	350.5	-8.3	13.85	13.25	13.21
J175021.86-414627.1	267.591	-41.774	349.4	-7.4	11.74	11.23	11.17
J175636.59-403545.9	269.152	-40.596	351.1	-7.9	12.86	12.29	12.19
J175433.19-411048.9	268.638	-41.180	350.4	-7.8	11.94	11.43	11.33

RA, right ascension; Dec., declination; *l* and *b*, Galactic longitude and latitude, respectively.

Journal of Cosmology (2015), Vol. 25, No. 32, pp 13613-13625.

Extended Data Table 2 | Stellar parameters of the 23 stars observed

Name (SMSS)	V_{helio} (km s^{-1})	$d_{\odot}$ (kpc)	$T_{\rm eff}$ (K)	$\log g$ (cgs)	[Fe/H] (dex)	ξ_t (km s^{-1})	[α/Fe] (dex)
J173823.38-145701.1	46.1	8.5	4599	0.99	-3.36	2.30	0.12
J182048.26-273329.2	51.5	6.0	4949	2.22	-3.48	1.90	0.37
J183744.90-280831.1	-132.6	17.6	4597	0.98	-2.92	2.05	0.33
J183647.89-274333.1	-381.4	6.6	4649	1.17	-2.48	2.50	0.30
J183812.72-270746.3	155.3	12.3	4873	1.74	-3.22	1.81	-0.01
J183719.09-262725.0	-244.7	10.0	4791	1.64	-3.18	1.81	0.32
J184201.19-302159.6	171.8	9.6	5136	2.55	-2.84	1.96	0.30
J184656.07-292351.5	91.0	9.5	4857	1.93	-2.76	1.83	0.34
J181406.68-313106.1	4.9	9.3	4821	1.48	-2.82	1.96	0.22
J181317.69-343801.9	139.3	6.5	5015	2.25	-2.28	1.48	0.41
J181219.68-343726.4	-386.2	8.0	4873	1.94	-2.50	1.93	0.32
J181609.62-333218.7	27.4	10.4	4809	1.93	-3.94	1.60	0.14
J181634.60-340342.5	-170.3	10.5	4821	1.61	-2.46	1.79	0.06
J175544.54-392700.9	-279.6	13.5	4857	1.83	-2.65	1.60	0.32
J175455.52-380339.3	23.5	13.5	4714	1.10	-3.36	1.80	0.08
J175746.58-384750.0	-59.4	9.1	5064	1.96	-2.81	2.36	0.29
J181736.59-391303.3	-177.9	15.7	4612	1.05	-2.59	2.09	0.32
J181505.16-385514.9	202.1	5.0	4962	2.73	-3.29	2.10	0.35
J181921.64-381429.0	-97.7	11.2	4917	2.02	-2.72	1.94	0.30
J175722.68-411731.8	63.8	12.4	4894	1.97	-2.88	2.02	0.19
J175021.86-414627.1	181.4	4.1	5015	2.12	-2.60	1.55	0.30
J175636.59-403545.9	-28.8	9.8	4934	1.79	-3.21	1.96	0.20
J175433.19-411048.9	-229.3	5.6	4912	1.91	-3.26	1.94	0.35

Symbols: $V_{\rm helio}$, heliocentric velocity; $d_{\odot}$, distance from the Sun to the star; $T_{\rm eff}$, effective temperature; log(g), stellar surface gravity; ξ_t, microturbulence; [α/Fe] = ([Mg/Fe] + [Ca/Fe] + [Ti/Fe])/3. Average uncertainties: velocity, 1.0 km s^{-1}; distance, 3.0 kpc; temperature, 160 K; microturbulence, 0.2 dex; log(g), 0.14 dex; [Fe/H], 0.09 dex; [α/Fe], 0.13 dex.

Extended Data Table 3 | Chemical abundances measured for each star, C to Ca

Name (SMSS)	A(Li)	[C/Fe]	[Na/Fe]	[Mg/Fe]	[Al/Fe]	[Si/Fe]	[K/Fe]	[Ca/Fe]
J173823.38-145701.1		0.49	0.04	0.17	-0.78	0.27		0.12
J182048.26-273329.2		0.98	-0.28	0.54	-0.63	0.96		0.30
J183744.90-280831.1	0.16	-0.20	-0.28	0.44	-0.52	0.58	0.36	0.25
J183647.89-274333.1		-0.47	-0.24	0.33	-0.66	0.51		0.18
J183812.72-270746.3	0.93	0.22	-0.39	0.05	-1.23	0.14		0.03
J183719.09-262725.0		0.40	-0.19	0.47	-0.77	0.36	0.41	0.25
J184201.19-302159.6		0.34	-0.38	0.26	-0.89	0.38	0.53	0.37
J184656.07-292351.5	1.04	0.08	-0.30	0.41	-0.95	0.36	0.58	0.28
J181406.68-313106.1		-0.51	0.18	0.23	-0.94	0.32		0.16
J181317.69-343801.9	1.05	0.17	-0.33	0.53	-0.82	0.33	0.63	0.34
J181219.68-343726.4	1.01	0.19	-0.22	0.30	-0.86	0.25		0.31
J181609.62-333218.7		$<$0.06	-0.01$<$0.91[a]	0.20	-1.08	0.54		0.00
J181634.60-340342.5		-0.10	-0.53	0.05	-1.08	0.11	0.21	0.03
J175544.54-392700.9	0.87	0.12	-0.32	0.29	-0.88	0.34	0.36	0.29
J175455.52-380339.3		-0.64		0.06	-0.88	0.30		0.03
J175746.58-384750.0		-0.04		0.37	-1.10	0.44		0.24
J181736.59-391303.3		-0.28	-0.11	0.38	-0.69	0.53	0.53	0.26
J181505.16-385514.9		0.23	-0.23	0.21	-0.96	0.15		0.36
J181921.64-381429.0	1.04	0.32	-0.24	0.28	-0.82	0.54	0.44	0.26
J175722.68-411731.8		0.42	-0.42	0.21	-0.70	0.48	0.14	0.13
J175021.86-414627.1	0.98	0.23	-0.37	0.30	-0.82	0.42		0.28
J175636.59-403545.9	0.93	0.65		0.30	-0.76	0.45		0.11
J175433.19-411048.9	0.92	0.24	-0.03	0.40	-0.74	0.43	0.44	0.32

A(Li) is the logarithmic abundance of lithium. All abundances are derived using LTE, except for Li, Na, Mg, and Ca, where non-LTE corrections have been applied. Average uncertainties: Li, 0.20; C, 0.25; Na, 0.20; Mg, 0.16; Al, 0.22; Si, 0.21; K, 0.17; Ca, 0.12.
[a]−0.01 is the lower limit, and 0.91 is the upper limit; see Methods for details.

RESEARCH LETTER

Extended Data Table 4 | Chemical abundances measured for each star, Sc to Cu

Name (SMSS)	[Sc/Fe]	[Ti/Fe]	[Cr/Fe]	[Mn/Fe]	[Co/Fe]	[Ni/Fe]	[Cu/Fe]
J173823.38-145701.1		-0.09	-0.22	-0.80	0.17	-0.21	<0.96
J182048.26-273329.2		0.16	-0.51	-0.97	0.24	-0.33	<1.33
J183744.90-280831.1	0.04	0.20	-0.23	-0.38	0.36	0.14	<0.29
J183647.89-274333.1	0.14	0.34	-0.27	-0.35	0.01	0.02	-0.43
J183812.72-270746.3		-0.20	-0.51	-0.32	0.22	-0.08	<1.06
J183719.09-262725.0	0.18	0.14	-0.33	-0.34	0.23	0.23	<1.10
J184201.19-302159.6	-0.03	0.20	-0.24	-0.57	0.35	-0.02	<0.72
J184656.07-292351.5	0.11	0.28	-0.19	-0.31	0.11	0.07	<0.45
J181406.68-313106.1	0.08	0.19	-0.30	-0.60	0.22	0.09	<0.50
J181317.69-343801.9	0.11	0.34	-0.19	-0.08	0.12	0.10	<0.13
J181219.68-343726.4	0.18	0.31	-0.15	-0.14	0.22	0.22	<0.17
J181609.62-333218.7		0.13	-0.65	-1.28	0.13	-0.11	<1.57
J181634.60-340342.5	-0.26	0.04	-0.24	-0.35	-0.20	-0.03	<-0.05
J175544.54-392700.9	-0.05	0.32	-0.22	-0.18	0.24	-0.05	<0.32
J175455.52-380339.3		0.02	-0.47	-1.05	0.07	-0.12	<0.85
J175746.58-384750.0	0.12	0.19	-0.44	-0.59	0.09	-0.01	<0.79
J181736.59-391303.3	0.15	0.24	-0.31	-0.34	0.00	0.08	<0.10
J181505.16-385514.9	0.40	0.38	-0.54	-0.81	0.17	-0.11	<1.02
J181921.64-381429.0	0.01	0.32	-0.17	-0.44	0.33	0.25	<0.50
J175722.68-411731.8	-0.22	0.15	-0.31	-0.48	-0.04	0.04	<0.82
J175021.86-414627.1	-0.23	0.26	-0.27	-0.31	0.16	0.16	<0.27
J175636.59-403545.9	-0.28	0.06	-0.29	-0.72	0.17	-0.26	<0.95
J175433.19-411048.9		0.22	-0.52	-0.91	0.29	0.02	<1.08

All abundances are derived using LTE. Average uncertainties: Sc, 0.10; Ti, 0.10; Cr, 0.21; Mn, 0.25; Co, 0.23; Ni, 0.19; Cu, 0.25.

Extended Data Table 5 | Chemical abundances measured for each star, Zn to Eu

Name (SMSS)	[Zn/Fe]	[Sr/Fe]	[Y/Fe]	[Zr/Fe]	[Ba/Fe]	[La/Fe]	[Eu/Fe]
J173823.38-145701.1	0.66	0.03	0.02	0.23	-0.04	-0.10	
J182048.26-273329.2	<1.01	-0.47			0.03	<1.33	
J183744.90-280831.1	0.27	-0.29	-0.32	0.03	-0.31	<0.12	
J183647.89-274333.1	0.23	0.18	-0.20	0.45	0.13	0.17	0.82
J183812.72-270746.3	<0.79	-1.03			-0.70	<0.77	
J183719.09-262725.0	0.48	0.04	0.53		-0.51	<1.03	
J184201.19-302159.6	<1.15	-0.20	0.04	0.70	0.16	<0.94	
J184656.07-292351.5	0.48	-0.26	-0.51	0.14	-0.32	<0.36	
J181406.68-313106.1	0.42	-1.61			-0.72	<0.32	
J181317.69-343801.9	0.17	0.17	-0.11	0.34	0.22	-0.09	0.15
J181219.68-343726.4	0.33	-0.06	-0.11	0.09	0.13	<0.90	0.48
J181609.62-333218.7	<1.40	-0.85	0.23		<-0.66	<1.09	0.91
J181634.60-340342.5	0.21	-0.25	-0.65	-0.21	-0.32	-0.14	-0.11
J175544.54-392700.9	0.36	-0.10	-0.2	0.38	-0.11	-0.15	0.21
J175455.52-380339.3	0.63	0.47	0.01	0.14	-0.57	<0.66	
J175746.58-384750.0		-0.21	0.04	0.91	0.23	<1.26	0.65
J181736.59-391303.3	0.23	-0.14	-0.47	0.14	-0.28	<1.19	0.21
J181505.16-385514.9	<0.95	-0.19	0.14	0.71	0.04	<0.54	0.96
J181921.64-381429.0	0.42	-0.21	-0.14	0.51	-0.01	0.48	0.59
J175722.68-411731.8	<0.95	-0.30	-0.30	0.24	-0.19	<0.63	0.52
J175021.86-414627.1	0.41	-0.14	-0.40	0.25	-0.08	<0.60	0.23
J175636.59-403545.9	0.86	0.55	0.24	0.71	-0.95	<1.21	
J175433.19-411048.9	0.50	-0.81	-0.29		-0.42	<0.91	

All abundances are derived using LTE. Average uncertainties: Zn, 0.10; Sr, 0.20; Y, 0.12; Zr, 0.12; Ba, 0.17; La, 0.15; Eu, 0.16.

Journal of Cosmology (2015), Vol. 25, No. 32, pp 13613-13625.

Extended Data Table 6 | Orbital parameters

Name (SMSS)	$\mu_\alpha \cos\delta$ (mas yr^{-1})	μ_δ (mas yr^{-1})	Mean r_{peri} (kpc)	Mean r_{ap} (kpc)	Mean Eccentricity	Mean Z_{max} (kpc)	E_{tot} (10^4 km^2 s^2)
J182048.26-273329.2	-4.10 $\pm$0.52	-6.38 $\pm$0.51	0.5 $^{+0.9}_{-0.2}$	2.9 $^{+1.7}_{-1.1}$	0.70 $^{+0.11}_{-0.23}$	0.9 $^{+0.2}_{-0.5}$	-11.3 $^{+2.2}_{-1.4}$
J184201.19-302159.6	-0.38 $\pm$0.90	-0.82 $\pm$0.90	1.2 $^{+1.1}_{-0.7}$	6.6 $^{+4.3}_{-1.6}$	0.72 $^{+0.13}_{-0.20}$	4.3 $^{+1.7}_{-1.8}$	-7.1 $^{+2.1}_{-1.2}$
J184656.07-292351.5	1.17 $\pm$0.89	-2.32 $\pm$0.89	1.2 $^{+1.5}_{-0.8}$	4.8 $^{+2.7}_{-1.4}$	0.65 $^{+0.19}_{-0.41}$	3.2 $^{+1.2}_{-1.4}$	-8.3 $^{+1.9}_{-1.2}$
J181406.68-313106.1	2.28 $\pm$0.52	-8.25 $\pm$0.52	1.1 $^{+2.3}_{-0.8}$	3.5 $^{+9.1}_{-1.3}$	0.63 $^{+0.18}_{-0.16}$	2.7 $^{+8.6}_{-0.8}$	-9.5 $^{+5.4}_{-1.8}$
J181219.68-343726.4	-2.42 $\pm$1.14	-1.29 $\pm$1.14	0.7 $^{+0.8}_{-0.4}$	17.3 $^{+11.3}_{-4.9}$	0.92 $^{+0.05}_{-0.03}$	7.2 $^{+3.2}_{-1.8}$	-3.4 $^{+1.9}_{-1.4}$
J181609.62-333218.7	-4.14 $\pm$0.64	-3.74 $\pm$0.64	1.0 $^{+3.5}_{-0.8}$	3.4 $^{+3.3}_{-1.8}$	0.53 $^{+0.23}_{-0.28}$	1.9 $^{+2.6}_{-0.9}$	-9.9 $^{+4.0}_{-2.6}$
J181634.60-340342.5	1.92 $\pm$0.62	-0.31 $\pm$0.62	1.9 $^{+2.0}_{-1.3}$	7.9 $^{+8.3}_{-2.4}$	0.65 $^{+0.15}_{-0.10}$	3.9 $^{+4.2}_{-1.7}$	-6.3 $^{+3.0}_{-2.0}$
J175544.54-392700.9	0.03 $\pm$1.49	-0.35 $\pm$1.46	1.7 $^{+2.3}_{-1.2}$	29.3 $^{+67.4}_{-16.5}$	0.92 $^{+0.05}_{-0.04}$	10.8 $^{+29.6}_{-6.0}$	-1.4 $^{+3.7}_{-3.2}$
J175455.52-380339.3	1.98 $\pm$1.14	4.76 $\pm$1.14	5.5 $^{+4.8}_{-3.9}$	811.5 $^{+1216.1}_{-796.2}$	0.98 $^{+0.01}_{-0.16}$	81.0 $^{+259.4}_{-76.6}$	6.9 $^{+12.2}_{-10.7}$
J175746.58-384750.0	1.86 $\pm$1.25	0.17 $\pm$1.25	1.8 $^{+1.9}_{-1.2}$	5.9 $^{+5.0}_{-1.9}$	0.59 $^{+0.24}_{-0.28}$	2.3 $^{+2.8}_{-1.1}$	-7.5 $^{+2.9}_{-1.8}$

Symbols: $\mu_\alpha \cos\delta$ and μ_δ are the proper motions in equatorial coordinates; r_{peri} and r_{ap} are the pericentric and apocentric radii of the orbit, respectively, Z_{max} is the maximum distance the orbit reaches above/below the Galactic plane, and E_{tot} is the total energy of the orbit. All values given here are the mean values from the Monte Carlo simulation of 1,000 orbits.